EPJ manuscript No.
(will be inserted by the editor)

Analytical study of chaos and applications

George Contopoulos, Mirella Harsoula and Christos Efthymiopoulos

Research Center for Astronomy and Applied Mathematics of the Academy of Athens
e-mail: gcontop@academyofathens.gr

arXiv:1603.09515v1 [nlin.CD] 31 Mar 2016

Abstract. We summarize various cases where chaotic orbits can be described analytically. First we consider the case of a magnetic bottle where we have non-resonant and resonant ordered and chaotic orbits. In the sequence we consider the hyperbolic Hénon map, where chaos appears mainly around the origin, which is an unstable periodic orbit. In this case the chaotic orbits around the origin are represented by analytic series (Moser series). We find the domain of convergence of these Moser series and of similar series around other unstable periodic orbits. The asymptotic manifolds from the various unstable periodic orbits intersect at homoclinic and heteroclinic orbits that are given analytically. Then we consider some Hamiltonian systems and we find their homoclinic orbits by using a new method of analytic prolongation. An application of astronomical interest is the domain of convergence of the analytical series that determine the spiral structure of barred-spiral galaxies.

1 Introduction

In generic nonintegrable dynamical systems there are both ordered and chaotic orbits. In particular ordered orbits appear near stable periodic orbits, while chaotic orbits appear near unstable periodic orbits (for a review see Contopoulos 2002).

Let us consider a system of two degrees of freedom with Hamiltonian

$$H = H(\rho, z, \dot{\rho}, \dot{z}) = H_2 + H_3 + \dots \tag{1}$$

where

$$H_2 = \frac{1}{2}(\dot{\rho}^2 + \dot{z}^2 + {\omega_1}^2\rho^2 + {\omega_2}^2 z^2) \tag{2}$$

and H_s contains terms of degree s.

Then the energy $H = E$ is an integral of motion around an equilibrium point $\rho = z = \dot{\rho} = \dot{z} = 0$. When the equilibrium is stable we can find another integral of motion around it

$$\Phi = \Phi(\rho, z, \dot{\rho}, \dot{z}) \tag{3}$$

but this is in general only formal. If we develop Φ in power series around the origin

$$\Phi = \Phi_2 + \Phi_3 + ... \tag{4}$$

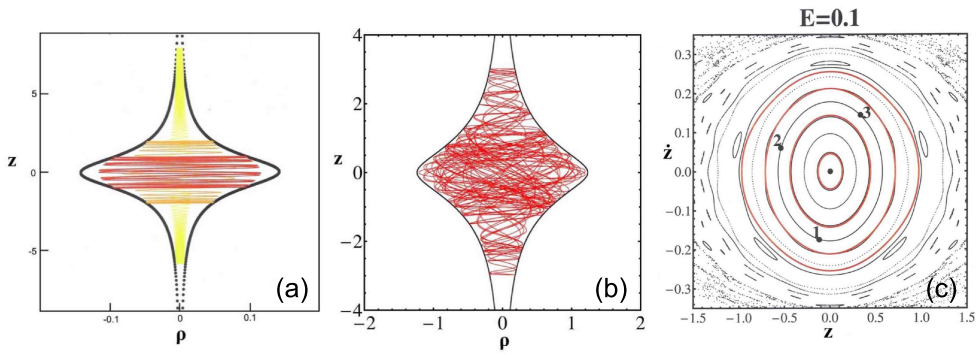

Fig. 1. Ordered and chaotic orbits in the magnetic bottle model. (a) 3 ordered orbits with different colours, (b) one chaotic orbit, (c) Invariant curves around the origin $O(0,0)$, numerical (black) and theoretical (red), for an energy $E = 0.1$. An orbit starting on an invariant curve (1) has its images (2, 3,...) on the same invariant curve.

and truncate this series at an order s the truncated integral, $\overline{\Phi}_s$, is better conserved as the order of truncation increases but only up to an optional order s_{opt}. However, if we include also higher order terms the approximation becomes worse. In fact the formal series Φ is divergent. Its divergence is due to the appearance of small divisors of the form $m_1\omega_1 + m_2\omega_2$ with m_1 , m_2 integers.

We can now solve the system (H, Φ_s) for a particular value of ρ (e.g. $\rho = 0$) and find a series

$$f(z, \dot{z}) = f_2 + f_3 + ... \tag{5}$$

that gives the successive points of an orbit on a Poincaré surface of section $(z, \dot{z})$.

A particular example that we studied recently (Efthymiopoulos et al. 2015), is the magnetic bottle Hamiltonian

$$H = \frac{1}{2}(\dot{\rho}^2 + \dot{z}^2) + \frac{1}{2}\rho^2 + \frac{1}{2}\rho^2 z^2 - \frac{1}{8}\rho^4 + \frac{1}{8}\rho^2 z^4 - \frac{1}{16}\rho^4 z^2 + \frac{1}{128}\rho^6 \tag{6}$$

which has the special feature that the second frequency ω_2 is zero. This Hamiltonian has been used in explaining the orbits generating the aurora near the poles of the earth. The orbits in the plane (ρ, z) are either ordered (Fig. 1a) or chaotic (Fig. 1b).

On a surface of section $(z, \dot{z})$ the ordered orbits are represented by invariant curves around the origin (Fig. 1c), or around a set of islands of stability (Fig. 2a,b). Namely the successive intersections of the orbit by the surface of section lie on a given invariant curve (Fig. 1c) or on successive islands (Fig. 2a,b). The theoretical invariant curves (red) found by using a truncated integral Φ_s of order $s = 12$ are very close to the numerical invariant curves (black) for small values of the energy (Fig. 1c). However for somewhat larger value of the energy there are islands of stability and the usual theoretical curves fail to represent these islands (Fig. 2a). The main new result of our recent paper (Efthymiopoulos et al. 2015) was that there exists a resonant form of the new integral Φ (in the case $\omega_2 = 0$) which represents very well the islands of a particular resonance (4/1 in the present case) and also the nonresonant invariant curves around the origin (Fig. 2b).

On the other hand for larger values of the energy the origin is unstable and around it there is an important chaotic region (Fig. 3a) (The intervals of the energy where the origin is unstable are given in the Appendix). Orbits in this chaotic region are chaotic and their successive intersections with the surface of section seem to be random.

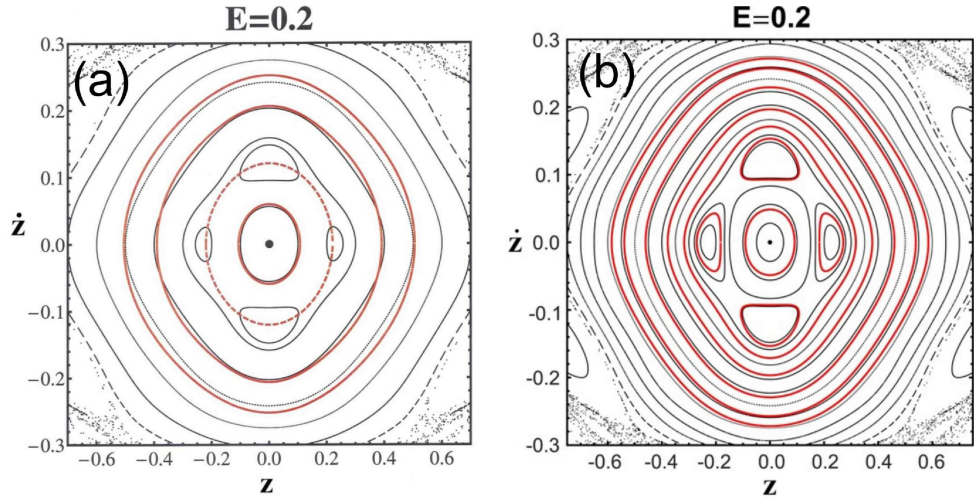

Fig. 2. Invariant curves for $E = 0.2$, numerical (black) and theoretical (red) for the Hamiltonian (6). (a) The nonresonant form of the integral Φ represents well the invariant curves around the origin, but not the islands. (b) The resonant form of the integral Φ represents both the invariant curves around the origin and the 4 islands.

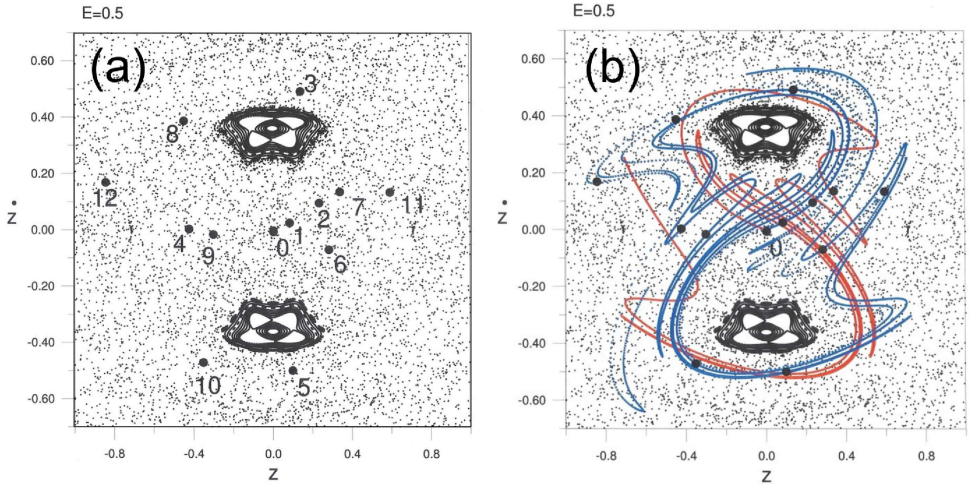

Fig. 3. When the energy is E=0.5 the central equilibrium $O(0, 0)$ is unstable. (a) Then the images of nearby initial conditions (point 1) seem to be scattered in a random way. (b) However as the point (1) is on the unstable asymptotic curve from O, all its images are on the same asymptotic curve (blue). (For comparison we give also the stable asymptotic curve (red))

However, around the unstable point at the origin, the new integral Φ is accurate (convergent) and not only formal. In fact, in the unstable case one frequency in the second order Hamiltonian (2) is real and the other is imaginary, thus no small divisors appear. This case was indicated already by Cherry (1926) and it was studied in detail by Moser (1956, 1958) and Giorgilli (2001).

In particular the asymptotic curves from the central unstable point (blue and red curves in Fig. 3b) are given by convergent series. Although these curves are

complicated, there are given theoretically with arbitrary accuracy. Thus, an orbit with initial conditions on an asymptotic curve has all its intersections on the same asymptotic curve. In this way the successive points 1,2,3,... etc of the orbit of Fig. 3a lie exactly on the unstable asymptotic curve (blue) emanating from the unstable periodic orbit O (Fig. 3b).

The problem that was not solved in the previous papers was to find the limits of the convergence of the series Φ. This subject was studied by us (Efthymiopoulos et al. 2014, Harsoula et al. 2015, Contopoulos and Harsoula 2015) in recent years and we describe its main points in sections 2 and 3. Then in section 4 we describe briefly some more recent results, namely an application to the chaotic spiral arms emanating from the Lagrangian points L_1, L_2 of barred spiral galaxies.

2 Moser invariant curves and chaos in mappings

A simple map that has an unstable point at the origin is the hyperbolic Hénon map (da Silva Ritter et al. 1987):

$$\begin{aligned} x' &= \cosh(\kappa)x + \sinh(\kappa)(y - \tfrac{x^2}{\sqrt{2}}) \\ y' &= \sinh(\kappa)x + \cosh(\kappa)(y - \tfrac{x^2}{\sqrt{2}}) \end{aligned} \tag{7}$$

When the parameter κ is equal to $\kappa = 1.43$ the eigenvalues of the origin ($x = y = 0$) are $\lambda_1 = e^{\kappa} = 4.1787$ and $\lambda_2 = 1/\lambda_1 = 0.2393$. A normal form series for the map (7) can be computed as follows: We change the variables to:

$$u = (x + y)/\sqrt{2} \ , \quad v = (x - y)/\sqrt{2} \tag{8}$$

and introduce a near identity transformation

$$\begin{aligned} u &= \Phi_1(\xi, \eta) = \xi + \Phi_{1,2}(\xi, \eta) + \Phi_{1,3}(\xi, \eta) + \dots \\ v &= \Phi_2(\xi, \eta) = \eta + \Phi_{2,2}(\xi, \eta) + \Phi_{2,3}(\xi, \eta) + \dots \end{aligned} \tag{9}$$

(where $\Phi_{i,s}$ $(i = 1, 2)$ contain the terms of s degree) such that the new variables (ξ, η) are transformed linearly

$$\xi' = \Lambda(c)\xi \ , \quad \eta' = \frac{1}{\Lambda(c)}\eta \tag{10}$$

with

$$\Lambda = \lambda_1 + w_2 c + w_3 c^2 + ... \ , \quad \frac{1}{\Lambda} = \lambda_2 + v_2 c + v_3 c^2 + ... \tag{11}$$

where

$$c = \xi\eta = constant \tag{12}$$

and w_s, v_s are constants independent of c.

Thus in the new variables (ξ, η) the hyperbolae (12) are invariant curves (Fig. 4a). The formulae that give the Moser transformations (9)-(11) are given by da Silva Ritter et al. (1987).

We found the domain of convergence of the series (9)-(11) by using the d' Alembert criterion (Efthymiopoulos et al. 2014). Namely we calculated the limits of the ratios

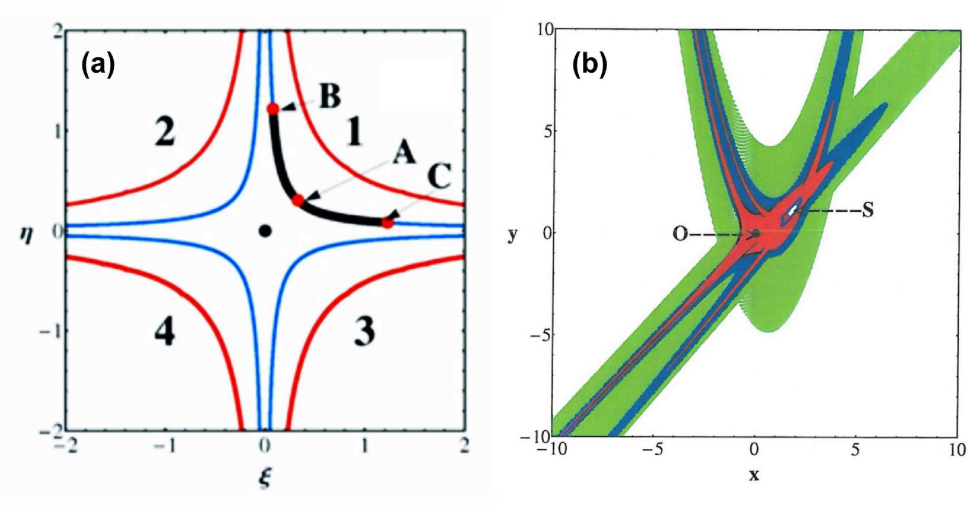

Fig. 4. (a) The invariant curves in the plane (ξ, η) are hyperbolae $c = \xi\eta$ in the sectors 1, 2, 3 and 4. A point on a hyperbola has its images and pre-images on the same hyperbola. B is the first image of A and C its first pre-image. (b) The Moser domain of convergence (red) in the variables (x, y) for $\kappa = 1.43$. S represents a stable periodic orbit. This is surrounded by a last KAM curve (black) and inside it is the inner limit of the Moser domain. All orbits with initial conditions outside the red region (in the intervals $-10 \leq x \leq 10, -10 \leq y \leq 10$) have their first images (green) and their second images (blue) approaching the boundaries of the domain of convergence.

$$\frac{|\Phi_{i,s}|}{|\Phi_{i,s+1}|} \tag{13}$$

along a given direction ϕ, where $\xi = R\cos\phi$ and $\eta = R\sin\phi$, in the (ξ, η) plane.

We found numerically that the limits of the ratio (13) depend on c but not on ϕ. For $\kappa = 1.43$ the series converge for $|c| \leq 0.49$. Thus the convergence domain in the plane (ξ, η) is limited by the hyperbolae $c = +0.49$ (regions 1 and 4 in Fig. 4a) and $c = -0.49$ (regions 2 and 3). Any orbit with initial conditions inside this domain, has its images and pre-images along a hyperbola passing through this point (Fig. 4a).

If we back-transform the hyperbolae of Fig. 4a to the original variables (x, y), using Eqs. (8)-(9), we find the image of the domain of convergence of the Moser series in the plane (x, y) (red in Fig. 4b). This domain is limited outwards by the images of the curves $c = \pm 0.49$ of the regions 2,3,4 of Fig. 4a. However there is also an inner limit, which is the image of the curve $c = 0.49$ of the region 1, in the (ξ, η) plane. Thus there is an inner region (white in Fig. 4b) where the series do not converge. This region is around a stable periodic point S.

In Fig. 5 we have drawn a number of invariant curves $\xi\eta = c$ as they are mapped in the variables (x, y). We call these curves "Moser invariant curves". In particular the curves $c = 0$ (red) represent the axes $\eta = 0$ and $\xi = 0$. These curves correspond to the stable and unstable asymptotic curves of the point $(0, 0)$ and extend to infinity within the domain of convergence, because the series (9) (and of course also (10)-(11)) converge all the way to infinity if $\eta = 0$ or $\xi = 0$. The images of the curves $\xi = 0$ and $\eta = 0$ intersect each other at an unlimited number of homoclinic points that can be found analytically.

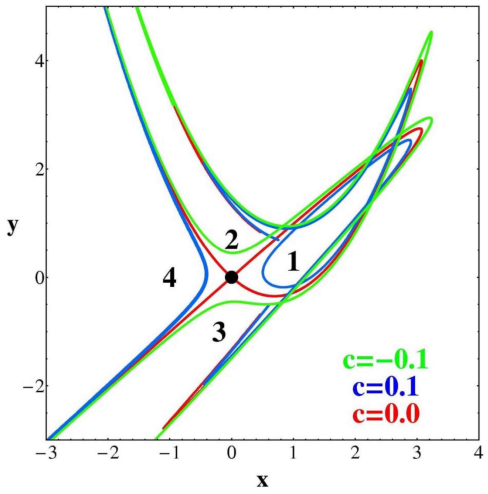

Fig. 5. A number of Moser invariant curves on the plane (x, y), that are images of hyperbolae of Fig. 4a in the sectors 1, 2, 3 and 4.

Any point in the domain of convergence of Fig. 4b has its images inside the same domain. On the other hand orbits with initial conditions outside the domain of convergence have images that approach closer and closer the outer limits of this domain. This is seen in Fig. 4b where we have mapped a grid of initial conditions $(-10, 10) \times (-10, 10)$ outside the convergence domain. Their first images are in green and their second images are in blue (covering also the inner green regions). Higher order images are congested even closer to the outer limits of the domain of convergence. Thus the outer limits of the domain of convergence act as an attractor for the orbits outside this domain.

The orbits close to the stable invariant point S are either ordered, forming invariant curves (KAM curves), or chaotic (around unstable periodic points of higher order). The KAM curves can be represented (approximately) by the usual series expansions around S of the form of the "third" integral (Contopoulos 2002). The last KAM curve (black curve in Fig. 6a) is outside the inner limit of the domain of convergence (blue curve). Between this limit and the last KAM curve there are Moser invariant curves, that are completely inside the last KAM curve (Fig. 6a). However, there are Moser curves that intersect the last KAM curve infinitely many times and extend very far from it (Fig. 6b). Finallly there are Moser invariant curves completely outside the last KAM curve (Fig. 6c).

In conclusion the Moser invariant curves are of three types (a) orbits completely inside the last KAM curve ($0.42 \lesssim c \lesssim 0.49$), (b) orbits intersecting the last KAM curve ($0.32 \lesssim c \lesssim 0.42$) and (c) orbits completely outside the last KAM curve ($c \lesssim 0.32$), It is of interest to note that the first type of Moser invariant curves contains both ordered orbits (and these orbits can be represented both by Moser series and KAM series), and chaotic orbits (that cannot be represented by KAM series). We emphasize that there is no contradiction in the fact that the Moser invariant curves are able to represent both ordered and chaotic orbits. For details see Harsoula et al. (2015). On the other hand inside the boundary ($c \geq 0.49$) i.e. closer to the point S the Moser series around the origin O do not converge, while there are KAM invariant curves that are represented (approximately) by the third integral type of series (but there are also small domains of chaotic orbits around high order unstable periodic orbits that cannot be represented by such series).

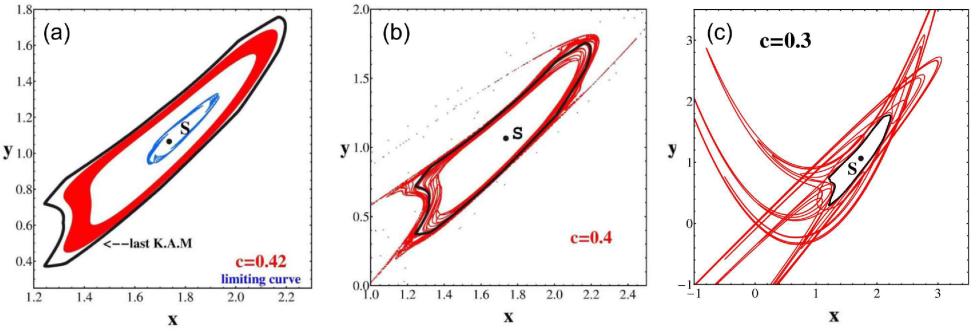

Fig. 6. (a) A Moser invariant curve (red) completely inside the last KAM curve (black) and outside the limiting curve (blue). (b) A Moser invariant curve intersecting the last KAM curve, infinitely many times, but extending also to large distances. (c) A Moser invariant curve completely outside the last KAM curve.

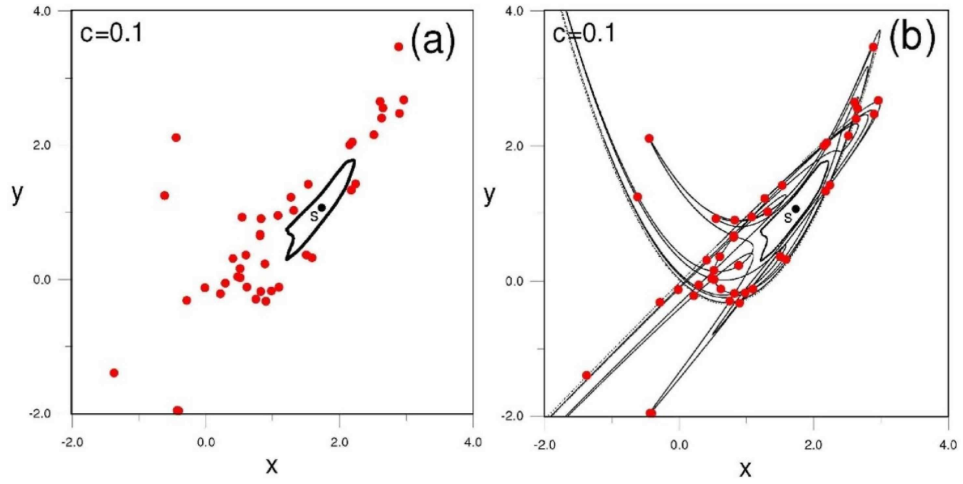

Fig. 7. (a) The images of a point close to the origin O are distributed in a random way. (b) However all these images lie on a particular Moser invariant curve.

The main application of the Moser series regards the orbits starting close to the origin O where chaos is dominant. In this case the successive images of an initial condition close to O look quite random (Fig. 7a). However, all these points lie on a particular Moser invariant curve curve (Fig. 7b) that can be given accurately analytically. Thus these orbits can be given by analytical formulae. The only indication of chaos is that although all the iterates lie on the same Moser curve, the distance between successive iterates increases at every iteration. Furthemore, the Moser invariant curves make many oscillations that extend to large distances, therefore some points on them may be at considerable distances from the center.

In this connection we must point out that the truncation error of the series is not uniform along the invariant Moser curves. In fact, at a fixed truncation order r, the error is small for the part of the hyperbola near the diagonal $\xi = \eta$, but it increases exponentially for the parts of the hyperbola approaching asymptotically the axes. As a consequence, we find that in order to accurately represent a segment of the hyperbola of length s around the diagonal using the Moser series we need to

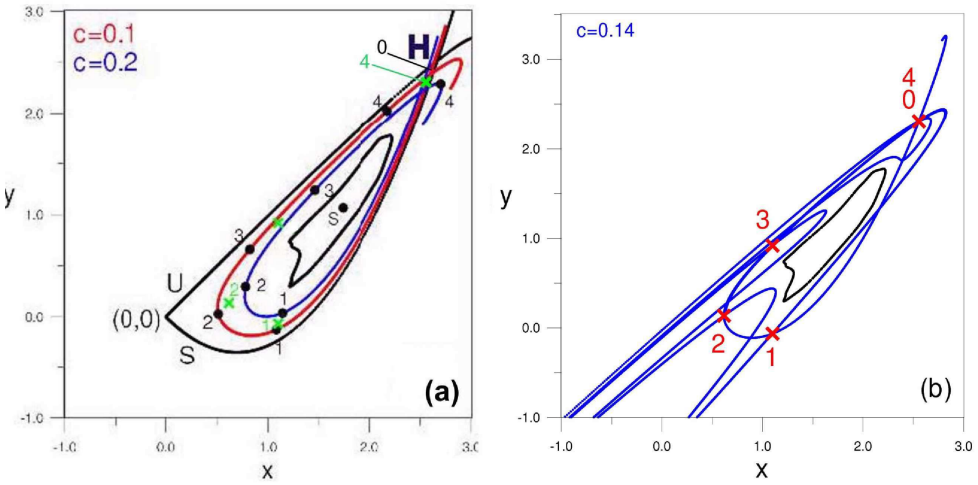

Fig. 8. (a) A method to find a periodic orbit of period 4 that has a point close to the homoclinic point H is the following: We use two invariant curves ($c = 0.1$ (red) and $c = 0.2$ (blue)) that intersect themselves close to H (point 0) and have images 1,2,3,4 where the point 4 is on the left of 0 for $c = 0.1$ and on the right of the corresponding intersection 0 for $c = 0.2$. Thus between them there is a periodic orbit $1, 2, 3, 4 \equiv 0$ of period 4 (green points). (b) An invariant curve (with $c \simeq 0.14$) that passes an infinite number of times from the 4 points of the periodic orbit of period 4.

reach a truncation order r which increases exponentially with s. This property is a manifestation of the exponential divergence of nearby chaotic orbits. Namely, in order to numerically integrate accurately a chaotic orbit up to a fixed time t, we need to know the initial conditions with a number of digits growing exponentially with t. On the other hand, in order to obtain analytically with a given precision a chaotic orbit up to a time t, we need to specify a number of coefficients in the series growing exponentially with t. Thus the chaotic character of the orbits manifests itself in the necessity to have either very accurate initial conditions (for a numerical calculation), or a large number of terms of the Moser series (for an analytical calculation).

A particular type of orbits along Moser invariant curves are the periodic orbits. In fact near the homoclinic points there is an infinity of periodic orbits. Such orbits were found by da Silva Ritter et al. (1987) in the following way. The homoclinic point H (Fig. 8a) has an infinity of images along the stable manifold of the periodic orbit $O(c = 0)$. Invariant curves with c close to zero intersect themselves at points near the homoclinic point H. The images of such a particular intersection (let us call it point 0) are the points 1, 2, ... If we join these points with the point S we form successive angles that have an average value (rotation angle) ϕ. If $\phi = 2\pi/n$ the n^{th} image coincides with 0 and we have a periodic orbit of period n.

In Fig. 8a we plot two invariant curves with $c = 1$ (red) and $c = 0.2$ (blue). The first curve has a rotation angle $\phi < 2\pi/4$ (the point 4 is on the left of the original point O) and the second curve has a rotation angle $\phi > 2\pi/4$ (its point 4 is on the right of the corresponding point O). Thus between these two curves there exists a curve with rotation number exactly $\phi = 2\pi/4$ and this is found by interpolation. The green points $1, 2, 3, 4 \equiv 0$ form a periodic orbit of period 4 with $c \simeq 0.14$. Closer to the homoclinic point H there are periodic orbits of period 5,6,... up to infinity. In fact the homoclinic points themselves can be considered as belonging to a periodic orbit with period $n = \infty$.

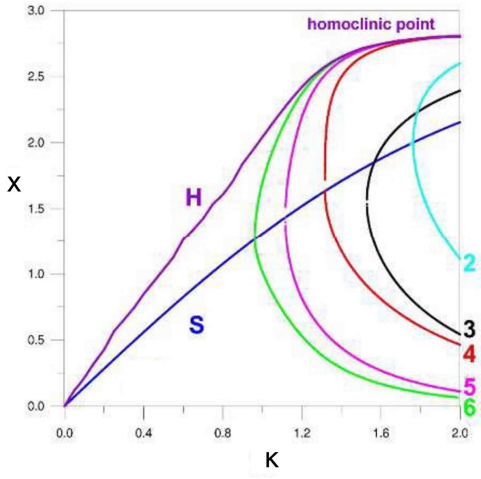

Fig. 9. Characteristics giving x as functions of κ for the families S, 6, 5, 4, 3 and 2, and for the homoclinic point H.

The invariant curve that passes through the four points of the periodic orbit with rotation number $\phi = 2\pi/4$, has many intersections with itself, but it passes an infinite number of times from the points $1, 2, 3, 4 \equiv 0$ (Fig. 8b). All the periodic orbits close to the homoclinic point H are unstable. These orbits were generated from the stable point S for smaller values of the parameter κ.

In Fig. 9 we give the characteristics of the various families 6,5,4,3,2 together with the characteristics of the periodic orbit S and of the homoclinic point H. The two families of period 4 are generated from the stable family S at $\kappa = 1.317$. The upper family is initially stable while the lower one is unstable. The stable family becomes unstable for $\kappa = 1.375$ at a period doubling bifurcation, and then all the families that were produced by a cascade of further bifurcations (with intervals between successive bifurcations decreasing by the universal ratio $\delta = 8.72$) become unstable beyond $\kappa = 1.383$. The same happens with all the families of order higher than 4. All these families are congested close to the homoclinic point H.

Of special interest are the families of period 2 because when these families are bifurcated from the original family S (for $\kappa = 1.76$), the orbit S itself becomes unstable. The stable family 2 becomes unstable at $\kappa = 1.84$ and then follows a cascade of periodic doubling bifurcations so that beyond $\kappa = 1.86$ all the bifurcated families become unstable.

When S becomes unstable it has its own asymptotic curves and new Moser invariant curves close to them. We found a Moser transformation that gives these new asymptotic invariant curves (Contopoulos and Harsoula 2015). We found also a Moser domain of convergence of these transformations which is completely inside the Moser domain of convergence around the orginial point O (Fig. 10a). In this case ($\kappa = 2$) there is no inner limit of the domain of convergence around O.

For $\kappa = 2$ the asymptotic curves from S intersect themselves at the homoclinic points H' and H'' (Fig. 10b). The eigenvalues of S are $\lambda_1 = -3.21$ and $\lambda_2 = 1/\lambda_1 = -0.31$, therefore this orbits is hyperbolic unstable. Then the successive points on the asymptotic curves are alternatively above and below S.

The asymptotic curves from the orbit S intersect the asymptotic curves from the orbit O at heteroclinic points. All the homoclinic and heteroclinic points are

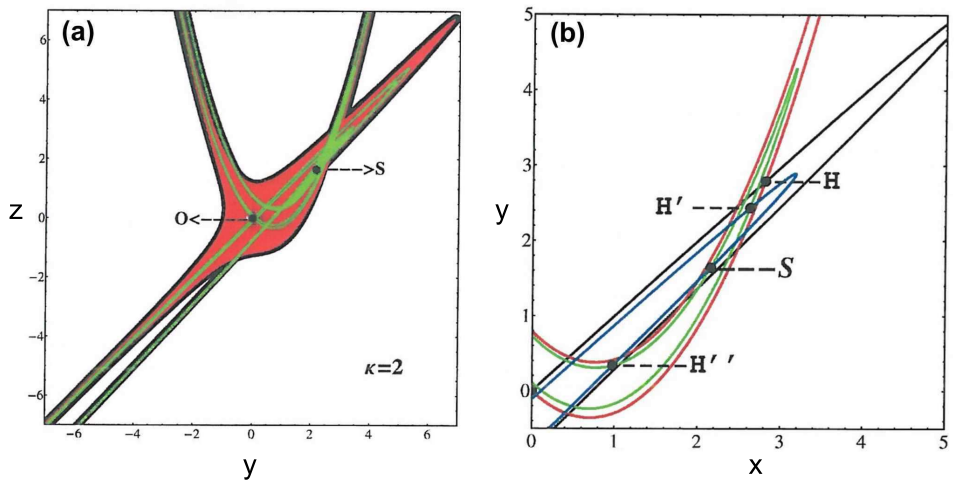

Fig. 10. (a) The Moser domains of convergence for orbits around O (red) and around S (green) for $\kappa = 2$. The green domain is completely inside the red domain. (b) The asymptotic curves from S, for $\kappa = 2$ intersect at homoclinic points H' and H''.

found analytically with a very good accuracy as compared with the numerical results (Contopoulos and Harsoula 2015).

The heteroclinic intersections do not appear immediately after the orbit S becomes unstable. In fact when S just becomes unstable there is still a last KAM curve around S, as it was when S was stable, and closed invariant curves inside it (but at a certain distance from S). Then the asymptotic curves from S remain for ever inside the last KAM curve. This situation occurs for a small interval of values of κ ($1.76 \leq \kappa \leq 1.79$). But when κ exceeds $\kappa = 1.79$ the last KAM curve around S is destroyed and the asymptotic curves from S intersect with the asymptotic curves from O.

Moser domains of convergence appear around every unstable periodic orbit. E.g. such domains of convergence appear around the unstable periodic orbit 2 that bifurcates from S and also when the stable orbit 2 becomes unstable. Thus we can imagine that the red Moser domain of convergence of Figs. 4b and 10a is full of smaller Moser domains of convergence around the various unstable orbits in the original domain. The corresponding orbits can be given analytically by more than one Moser series. This has been checked in cases where we have intersections of Moser invariant curves around O with curves around S (Contopoulos and Harsoula 2015).

Our conclusion is that inside the Moser domains, where most orbits are chaotic we can find analytic expressions for such orbits and describe in detail their chaotic behavior.

3 Hamiltonian Systems

While in simple mappings, like the hyperbolic Hénon map, the convergence along the asymptotic curves of a hyperbolic orbit goes to infinity, in Hamiltonian systems the convergence extends only up to a finite distance. Thus, it is not certain that one can find analytically the homoclinic intersections of the asymptotic curves. In fact although Vieira and Ozorio de Almeida (1996) and Bongini et al (2001) applied the method of Moser in hamiltonian cases, they could not find even the first homoclinic

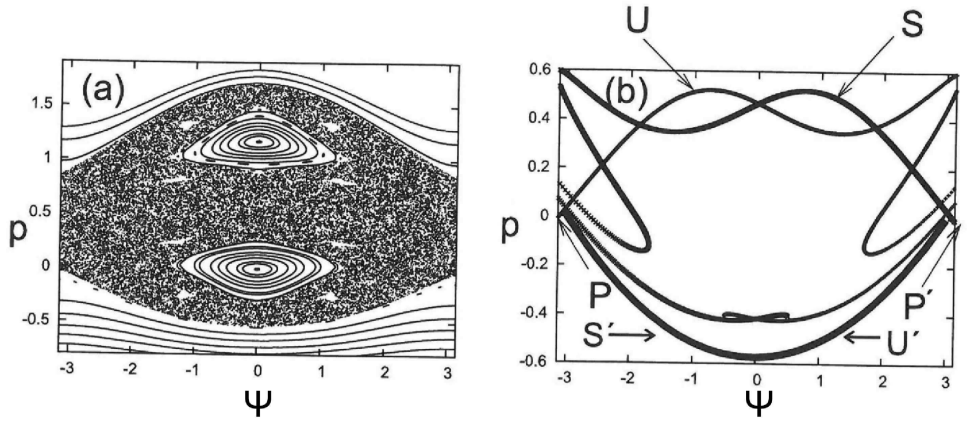

Fig. 11. (a) The surface of section (Ψ, P) for orbits in the Hamiltonian (14) for $\epsilon = \omega = 1$ and ${\omega_0}^2 = 0.08$. Most orbits in a domain around $p = 0$ are chaotic. (b) The asymptotic curves from the periodic orbit (P at $\psi_0 = -\pi$) (which is the same as the orbit P' at $\psi_0 = \pi$.)

point. They only approached it when the Moser series was truncated at high orders. However by applying a method of analytic continuation we could extend the applicability of the Moser method and calculate theoretically several homoclinic points (Efthymiopoulos et al. 2014).

As an example we used the Hamiltonian

$$H = \frac{1}{2}p^2 - {\omega_0}^2[1 + \epsilon(1 + p)\cos\omega t]\cos\psi \tag{14}$$

which represents a perturbed pendulum. For $\epsilon = 0$ we have the Hamiltonian of a pendulum

$$H = \frac{1}{2}p^2 - {\omega_0}^2\cos\psi \tag{15}$$

If we use a dummy action I, conjugate to the angle $\phi = \omega t$ we can write an equivalent Hamiltonian

$$H = \frac{1}{2}p^2 + \omega I - {\omega_0}^2[1 + \epsilon(1 + p)\cos\phi]\cos\psi \tag{16}$$

For $\epsilon = \omega = 1$, ${\omega_0}^2 = 0.08$ a Poincaré surface of section is given in Fig. 11a by taking $\phi = 2\pi n$, ($n = 0, 1, 2, ...$). Most of the central region of Fig. 11a is chaotic, but there are also some islands of stability near the axis $\psi = 0$ and also regular orbits above and below the chaotic domain. The chaotic behaviour is around the asymptotic curves from the unstable periodic orbit $P(mod 2\pi)$ (P at $\psi_0 = -\pi$ or P' at $\psi_0 = \pi$). These asymptotic curves intersect at an infinity of homoclinic points above and below the axis PP'. (The stable and unstable asymptotic curves undergo large oscillations in the upper part of Fig. 11b, but smaller oscillations in the lower part.)

We measure now the angles u from the point $\psi_0 = \pi$, i.e. we have $\psi = u - \pi$. If we develop $\cos\psi$ in powers of u we find

$$H = \frac{1}{2}p^2 + \omega I + 0.08[1 + \epsilon(1 + p)\cos\phi][1 - \frac{u^2}{2} + \frac{u^2}{24} - \ldots] \tag{17}$$

The lowest order term of this Hamiltonian is

$$H_0 = \frac{1}{2}(p^2 - {\omega_0}^2 u^2) \tag{18}$$

and if we use diagonal variables (ξ, η) through

$$p = \frac{\sqrt{\omega_0}(\xi + \eta)}{\sqrt{2}} \quad u = \frac{(\xi - \eta)}{\sqrt{2\omega_0}} \tag{19}$$

we find

$$H_0 = \omega_0 \xi \eta \tag{20}$$

Thus the Hamiltonian (15) becomes

$$H = \omega I + \omega_0 \xi \eta + H_1 \tag{21}$$

where H_1 is the perturbation $H_1 = H_1(\phi, I, \xi, \eta)$ (In this particular case H_1 does not depend on I).

Then we find new variables (ϕ', I', ξ', η') such that

$$H = \omega I' + {\omega_0}' \xi' \eta' + Z(I', \xi' \eta') \tag{22}$$

i.e the perturbation depends only on I' and on product $c = \xi' \eta'$ and does not depend on ϕ'.

Then the quantities I' and $c = \xi' \eta'$ are integrals of motion. The transformations

$$(\phi, I, \xi, \eta) = \Phi(\phi', I', \xi', \eta') \tag{23}$$

are given by a normalization method in the form of series (Efthymiopoulos et al. 2014).

In these variables the successive iterates in the plane (ξ', η') are along hyperbolae. In particular the asymptotic curves are the axes $\eta' = 0$ and $\xi' = 0$ (Fig. 12). On the other hand in the original variables (ξ, η) the asymptotic curves are curved and intersect at homoclinic points like H_0. If now we come back to the original variables (ψ, p) on the surface of section we find curves that are similar to the curves U and S of Fig. 11b close to the origin (Fig. 13), but further away they deviate considerably. If we increase the order of the normalizing series (22) we approach closer to the homoclinic point H_0 but do not reach it. This is due to the fact that the convergence of the series is limited up to two points A and A' along the asymptotic curves.

In fact the series giving the variables (ϕ, I, ξ, η) in terms of (ϕ', I', ξ', η') converge in the complex plane of Ψ up to a limit $|Im(\Psi)| \leq \sigma$, $\sigma > 0$ while the real values $Re(\Psi)$ vary from 0 to 2π.

In order to overcome this difficulty, which is due to the limits of the convergence, we use the following method (Efthymiopoulos et al. 2014). If we have a point a on the ξ-axis of Fig. 12, where the Moser formulae do not converge, we find a pre-image a' close to the origin (say the m-th preimage), where the series converge and we find the corresponding point a' on the plane (ξ, η). Then by proceeding in steps along which there is no convergence problem we proceed from a' to its m-th image, which is the required image A of a. In the same way we proceed from a point b along the axis η to find its image B. The images and the pre-images can be found by a series based on the Lie operator defined by the Hamiltonian (15). Thus, the whole method corresponds to a method of analytic continuation that allows us to go beyond the limits of convergence of the original series due to singularities in the complex domain.

Using this method in the problem of the perturbed pendulum with $m = 3$ and 4 steps (4 successive transformations) we could find in Fig. 14 accurately the asymptotic

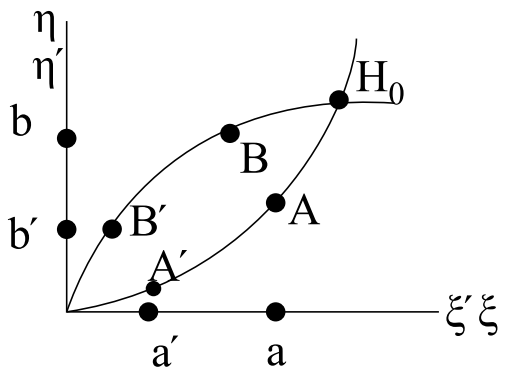

Fig. 12. The asymptotic curves in the variables (ξ', η') are the axes $\xi' = 0$ and $\eta' = 0$, while in the variables (ξ, η) they are curves intersecting at the homoclinic point H_0 (schematically). A point α in on the ξ' axis beyond the convergence domain has an $m - th$ preimage α' inside the convergence domain, whose image on the (ξ, η) plane is the point A'. Then the $m - th$ image of A' is A. Thus A can be found by analytic formulae as the image of α. Similary B is the image of b.

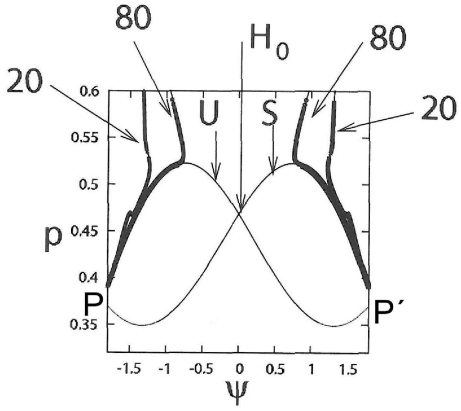

Fig. 13. The Moser series for the invariant curves from the point P (U = unstable) and P' (S=stable) truncated at orders 20 and 80 are close to the numerical asymptotic curves up to some distance but then they deviate considerably and do not approach very close the homoclinic point H_0.

curves that were computed numerically in Fig. 11b up to at least 9 homoclinic points $(H_0, H_1, H_2, H_3, H_4, H_{-1}, H_{-2}, H_{-3}, H_{-4})$.

The conclusion from the above studies is that in principle we can find analytically the asymptotic curves (and nearby invariant curves) up to an arbitrarily large length. Thus we can find analytically the chaotic orbits for an arbitrarily long time. However, in practice we have computational limitations related to the growing complexity of the series.

4 Application to barred spiral galaxies

A particular application of this new method has been made recently (Harsoula et al. 2015), in order to connect the Moser domain of convergence around the Lagrangian

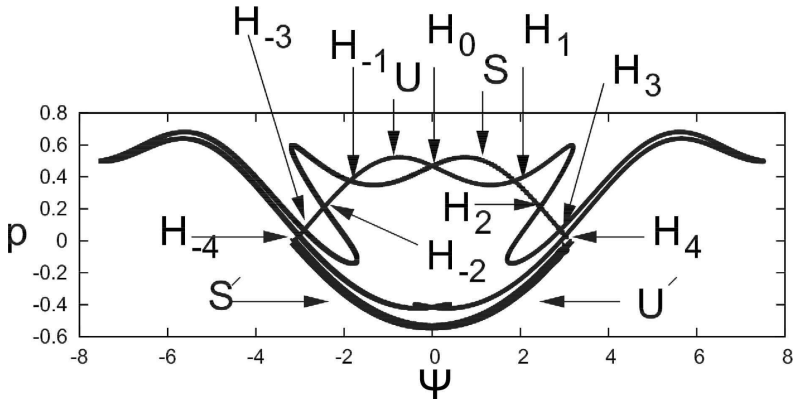

Fig. 14. Our new method allows the calculation of the Moser invariant curves up to a large extent, allowing the analytical calculation of the homoclinic points $H_0, H_1, H_2, H_3, H_4, H_{-1}, H_{-2}, H_{-3}, H_{-4}$.

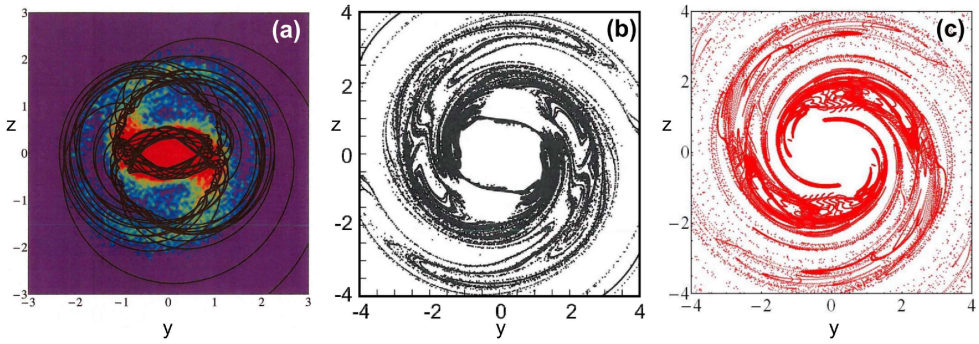

Fig. 15. (a) The N-body surface density of a N-body simulation of a barred galaxy (colours) shows the bar and the spiral arms emanating from the ends of the bar. Superimposed is an orbit starting close to the Lagrangian point L_1. (b) The apocentric manifolds from the ends of the bar define the basic structure of the spiral arms. (c) The spiral arms generated by the theoretical asymptotic curves and their neighbourhoods are quite close to the numerical asymptotic curves of Fig. 15b.

points L_1 and L_2 of barred-spiral galaxies with the chaotic spiral arms beyond them. A particular N-body simulation of a barred-spiral galaxy produced by Voglis et al. (2006) (named model QR2), shows a concentration of stars along spiral arms emanating from the ends of the bar (Fig.15a). The orbits of the stars supporting the spiral arms are chaotic. A particular chaotic orbit starting close to L_1 is superimposed in Fig.15a. This orbit stays for a long time (compared to a Hubble time), close to the spiral arms and the outer parts of the bar, before escaping from the system. In general the stars stay longer close to the apocentra (or pericentra) of their orbits. Therefore the apocentra (or pericentra) define the spiral arms (Fig. 15b) which are density waves, i.e. the stars of the spiral arms are continuously replaced by other stars.

We now apply the method described in the previous sections to find the analytical asymptotic curves emanating from the Lagrangian points L_1 and L_2 at the end of the bar (Fig. 15c). These analytical asymptotic curves and the Moser invariant curves close to them make many oscillations, back and forth, but their overall form is very

similar to the distribution of the apocentra (and pericentra) of the orbits shown in Fig. 15b. The details of these calculations will be given in a future paper.

A simple theoretical model of the spiral arms is provided by finding an averaged Hamiltonian and a corresponding mapping, using a method introduced by Hadjidemetriou (1991, 2008). We start with a Hamiltonian representing the N-body, distribution on the plane of rotation, of the form:

$$H = \frac{{p_r}^2}{2} + \frac{{p_\phi}^2}{2r^2} - \Omega_p p_\phi + \Phi(r,\phi) \tag{24}$$

where r and ϕ are polar coordinates, in a frame rotating with pattern velocity Ω_P and p_r, p_ϕ are the corresponding momenta. The potential Φ consists of an axisymmetric part Φ_0 and a mode $m = 2$ in the form

$$\Phi = \Phi_0(r) + \Phi_1(r)\cos 2\phi + \Phi_2(\phi)\sin 2\phi \tag{25}$$

Then we develop the Hamiltonian around the corotation radius r_0 setting $r = r_0 + \delta r$, $p_\phi = p_0 + J_\phi$, and introduce a pair of action angle variables (J_r, ϕ_r) by the transformation

$$\delta r = \sqrt{2J_r/\kappa_r}\sin(\phi_r), p_r = \sqrt{2\kappa_r J_r}\cos(\phi_r) \tag{26}$$

where κ_r is the epicyclic frequency given by the formula:

$$\kappa_r = \sqrt{\partial \Phi_{eff}^2/\partial r^2} \tag{27}$$

with an effective axisymmetric component

$$\Phi_{eff} = \frac{{p_0}^2}{2r^2} + \Phi_0(r) \tag{28}$$

Thus we derive a Hamiltonian $H = H(J_\phi, \phi, J_r, \phi_r)$. Then we average this Hamiltonian over the angles ϕ_r, while J_r is a constant. The orbits in this averaged Hamiltonian are found by solving the equations of motion.

We then use the Hadjidemetriou method (1991,2008), which consists of finding a 2D-mapping that has the same fixed points and the same stability indices with the given Hamiltonian. In our particular case of a galaxy, we find an approximate mapping for this system, which is the standard map

$$x_1' = x_1 + x_2' \ , \quad x_2' = x_2 + K\sin(x_1) \tag{29}$$

(without the modulo 2π). In the case of the model QR2 of Voglis et al. (2006), we find that the value of K is $K = 2.68488$.

The origin of this standard map corresponds to the Lagrangian point L_1 (or L_2) of the spiral Hamiltonian. This point is an unstable periodic orbit, and we can now apply the Moser theory around it. Namely we find a transformation to new variables (ξ, η) in which the mapping is

$$\xi' = \Lambda(c)\xi \ , \quad \eta' = \frac{1}{\Lambda(c)}\eta \tag{30}$$

where

$$\xi'\eta' = \xi\eta = c(constant) \tag{31}$$

i.e. the mapping is along hyperbolae in the variables (ξ, η). The formulae giving the variables (x, y) are convergent whenever $|\xi\eta| = |c|$ is smaller than a critical value

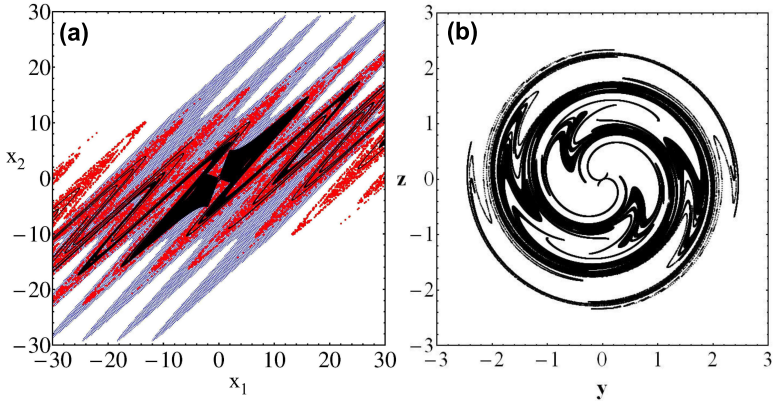

Fig. 16. (a) The Moser domain in the variables (x, y) (black), and the first and third iterates of a grid of initial conditions $(-20 < x_1 < 20\ ,\ -20 < x_2 < -20)$ (blue and red respectively.) (b) The Moser domain of convergence in the cofiguration space of the galaxy.

$c_{crit} \backsimeq 4$. The image of the domain of convergence $|\xi\eta| \leq c_{crit}$ in the plane (x_1, x_2) is called now a "Moser domain". The most important result is the following: While in the variables (x_1, x_2) of the standard map the Moser domain is given as a black region in Fig. 16a, in the original variables (y, z) of the configuration space of the galactic model, the Moser domain has a spiral form (Fig. 16b).

It is of great interest that the theoretical form of the spirals, as given by the Moser domain, is very close to the observed spirals of the N-body simulation. The details of these calculations are given in Harsoula et al. (2016).

Finally, we take initial conditions outside the Moser domain we find that their iterates approach the outer limit of the Moser domain. This can be seen in Fig. 16a where we have taken a dense grid of initial conditions with $-20 < x_1 < 20, -20 < x_2 < 20$ that fill an area larger than the limits of the N-body system. The first iterates of these initial conditions (blue) approach the Moser domain and the third iterates (red) approach it even closer (Fig. 16a). Higher order iterates approach very close the boundary of the Moser domain. Thus the boundary of the Moser domain acts as an attractor for the orbits that start outside this domain. On the other hand orbits starting inside the Moser domain cannot ever go outside it.

The fact that the boundary of the Moser domain acts as an attractor was found first in the case of a different mapping (the hyperbolic Hénon map) by Contopoulos and Harsoula (2015). Thus, it seems that this phenomenon is quite general.

On the other hand we can see in Fig. 16a that the Moser domain extends to larger values of x_1 and x_2 as the number of iterations increases. In this way the orbits can go to large distances and eventually they escape to infinity. However the orbits remain close to the spiral arms of the galaxy for a long time before escaping to infinity. This means that the chaotic orbits outside corotation remain sticky close and along the asymptotic manifolds for a long time before allowing their orbits to escape.

Our conclusion is that the asymptotic curves (manifolds) from the unstable periodic orbits (and the nearby invariant curves) that are given by analytical formulae can have important applications in particular problems of interest.

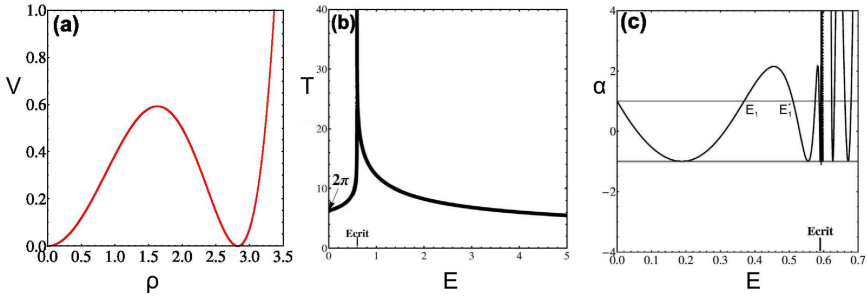

Fig. 17. (a) The function $V(\rho, 0)$. (b) The period T of the orbits passing through the origin ($\rho = \Delta$) as a function of the energy E. (c) The Hénon stability index for the orbits passing through the origin ($\rho = 0$) as a function of the energy E.

A Appendix: Intervals of instability of the central periodic orbit

The central periodic orbit $z = 0$ of the magnetic bottle given by the Hamiltonian (6) is stable for $0 < E < 0.366882$. Beyond this energy, this periodic orbit becomes unstable for an interval ΔE_1 and then undergoes transitions from stability to instability and vice versa as the energy approaches a critical value $E_{crit} = 0.592593$ at which the period tends to infinity. In fact the period of the orbit $z = 0$ is found from the equation

$$\frac{1}{2}\dot{\rho}^2 + V(\rho, 0) = E \tag{32}$$

where

$$V(\rho, 0) = \frac{1}{2}\rho^2 - \frac{1}{8}\rho^4 + \frac{1}{128}\rho^6 \tag{33}$$

The function $V(\rho, 0)$ (Fig. 17a) has a maximum $E = E_{crit} = 0.592593$ for $\rho_{max} = \rho_{crit} = 1.692993$. The period is twice the time to go from $\rho_{min}(= -\rho_{max})$ to ρ_{max}, where ρ_{max} is the root of the equation $V(\rho, 0) = E$, i.e.

$$T = 2\int_{\rho_{min}}^{\rho_{max}} \frac{d\rho}{\sqrt{2(E - V(\rho, 0))}} \tag{34}$$

When E decreases and tends to zero the period decreases and tends to $T = 2\pi$ and when $E \to E_{crit}$ it tends to infinity (Fig. 17b). For $E > E_{crit}$ the period decreases and tends to zero when the energy tends to infinity (Fig. 17b).

In order to find the stability of the periodic orbit $z = 0$ we calculate the Hénon stability index α. The orbit is stable if $-1 < \alpha < 1$ and unstable if $a > 1$ (or $a < -1$) (Fig. 17c). We see that as E approaches E_{crit} we have an infinity of intervals $(E_n, E_n{}')$ inside which the orbit is unstable (Table I).

Table I			
n	E_n	$\Delta E_n = \|E_n - E_{crit}\|$	$\delta = \frac{\Delta E_n}{\Delta E_{n+1}}$
1	0.366882	0.225711	13.03
2	0.5752725	0.017320	15.073
3	0.5914435	0.00114959	15.181
4	0.5925169	0.0000756926	15.176
5	0.592587605	4.98759 x 10^-6	15.20
6	0.592592264575	3.28017 x 10^-7	15.188
7	0.592592570995	2.1597 x 10^-8	-

In particular the value $E = 0.5$ of Fig. 3a is in the interval $(E_1, E_1{}')$ where the orbit $z = 0$ is unstable.

The phenomenon of infinitely many transitions to instability and stability was first observed by Churchill et al (1980) and by Contopoulos and Zikides (1983). Then Heggie (1983) has shown that the distances ΔE_n of the successive energies E_n where we have transitions to instability from the critical energy E_{crit} decrease by a factor

$$\delta = \frac{|E_n - E_{crit}|}{|E_{n+1} - E_{crit}|} \tag{35}$$

which tends to a limiting number

$$\delta = exp\left[\pi\sqrt{\left|\frac{V_{\rho\rho}}{V_{zz}}\right|}\right]_{\rho=\rho_{max},z=0} \tag{36}$$

where V_{pp} and V_{zz} are the second derivatives of V with respect to ρ and z.

In the present case the theoretical value of Eq. (36) is $\delta = 15.19$. If we compare this value with the numerical ratios of Table I we find that indeed the values of δ tend to this theoretical value as the order n increases.

On the other hand for large values of E the periodic orbit $z = 0$ is unstable. As E decreases this orbit becomes stable for the first time at $E = 4.098$. As E decreases further and tends to E_{crit} we have an infinity of transitions from instability to stability (Fig. 17c). However in this case the ratio δ does not tend to $\delta = 15.19$ as in the case of energies $E < E_{crit}$ for orbits around the origin.

References

1. Bongini, L., Bazzani, A. and Turchetti, G., Phys. Rev. Sp. Topics **4**, (2001) 114201
2. Cherry, T.M., Proc. London Math. Soc. Ser. 2 **27**, (1926) 151
3. Churchil, R.C., Pecelli, G. and Rod D.L, Archive for Rotational Mechanics and Analysis **73**, (1980) 313
4. Contopoulos, G. and Zikides, M., Astron. Astrophys. **20**, (1980) 198
5. Contopoulos, G., *Order and Chaos in Dynamical Astronomy* (Springer-Verlag, 2002)
6. Contopoulos, G. and Harsoula, M., J. Phys. A **48** (2013) 335101
7. Da Silva Ritter, G.I., Ozorio de Almeida, A.M. and Douandy, R., Physica D **29**, (1987) 181
8. Efthymiopoulos, Ch., Contopoulos, G. and Katsanikas, M., Celest. Mech. Dyn.Astron. **119**, (2014) 321
9. Efthymiopoulos, Ch., Harsoula, M. and Contopoulos, G., Nonlinearity **28**, (2015) 851
10. Giorgilli A., Disc. Cont. Dyn. Sys. **7**, (2001) 855
11. Hadjidemetriou, J. D., in *Predictability, stability and chaos in N-Body Dynamical Systems* (Plenum Press, New York, 1991) 157
12. Hadjidemetriou, J. D., Non Lin. Phen. in Complex Systems **11**, (2008) 149

13. Harsoula, M., Contopoulos, G. and Efthymiopoulos, Ch., J. Phys. A **48**, (2015) 135102
14. Harsoula, M., Efthymiopoulos, Ch. and Contopoulos, G., *in preparation* (2016)
15. Heggie, D. C., Celest. Mech. Dyn.Astron. **29**, (1983) 207
16. Moser, J., Commun. Pure Applied Math. **9**, (1956) 673
17. Moser, J., Commun. Pure Applied Math. **11**, (1958) 257